Operando Nanoindentation: A New Platform to Measure the Mechanical Properties of Electrodes during Electrochemical Reactions

Luize Scalco de Vasconcelos, Rong Xu, and Kejie Zhao[*,z]

School of Mechanical Engineering, Purdue University, West Lafayette, Indiana 47907, USA

We present an experimental platform of operando nanoindentation that probes the dynamic mechanical behaviors of electrodes during real-time electrochemical reactions. The setup consists of a nanoindenter, an electrochemical station, and a custom fluid cell integrated into an inert environment. We evaluate the influence of the argon atmosphere, electrolyte solution, structural degradation and volumetric change of electrodes upon Li reactions, as well as the surface layer and substrate effects by control experiments. Results inform on the system limitations and capabilities, and provide guidelines on the best experimental practices. Furthermore, we present a thorough investigation of the elastic-viscoplastic properties of amorphous Si electrodes, during cell operation at different C-rates and at open circuit. Pure Li metal is characterized separately. We measure the continuous evolution of the elastic modulus, hardness, and creep stress exponent of lithiated Si and compare the results with prior reports. operando indentation will provide a reliable platform to understand the fundamental coupling between mechanics and electrochemistry in energy materials.

[DOI: 10.1149/2.1411714jes]

Manuscript submitted October 23, 2017; revised manuscript received December 4, 2017. Published December 19, 2017.

Mechanics and electrochemistry are intimately coupled in energy technologies such as batteries,[1,2] fuel cells,[3,4] supercapacitors,[5,6] photovoltaics,[7] and hydrogen storage.[8] The electrochemical reactions between the host material and guest species induce deformation, stress, fracture, and fatigue which cause ohmic and thermal resistance increase, and performance degradation. Likewise, mechanical stresses regulate mass transport, charge transfer, interfacial reactions, and consequently the potential and capacity of electrochemical systems.[9] In batteries, mechanical degradation compromises the performance of current technologies[10–12] and limits the implementation of high-capacity electrodes.[13,14] Mechanics of both anode and cathode materials, such as diffusion-induced stresses, large deformation, plasticity, and fracture, have been extensively studied in recent years.[15–20] Nevertheless, the intimate coupling between mechanics and electrochemistry is far from complete understanding despite a considerable volume of existing studies. One major deficiency is the lack of reliable experimental tools to characterize the mechanical behaviors of electrodes under real electrochemical conditions. The operation of batteries is extremely sensitive to the work environment – a trace of oxygen and moisture can cause numerous side reactions. In contrast, most mechanical test equipment is open system with limited capability of environment control. As such, the mechanics and electrochemistry of batteries are often characterized separately. Recent studies propose that the mechanical response of materials at the chemical equilibrium states may differ from that under concurrent mechanical and chemical loads.[21,22] There is an urgent need for an experimental platform to probe the chemomechanical behaviors of electrodes in the course of electrochemical reactions.

Current experimental tools have been able to provide valuable insight. Due to the generally small characteristic size and heterogeneous feature of electrodes, large-scale mechanical tests find limited applications in energy materials, restricting most relevant measurements to the nano- and micro-scales. The wafer-curvature method is a convenient and reliable tool to measure the stress evolution in thin-film electrodes during electrochemical cycles. This technique has been used to monitor the stress development in Ge,[23] Si,[24] metal oxides,[25,26] and composite thin films[27] at a specific states-of-charge. Nevertheless, it is not convenient to map the continuous evolution of mechanical properties (elastic modulus, hardness, viscous property) of electrodes upon Li reactions, or to probe the local variations in a composite configuration by wafer-curvature measurements. Another method to determine the mechanical properties in a controlled environment is tensile tests of nanowires. Kushima et al., for instance, performed delicate tensile experiments of fully lithiated Si nanowires inside a transmission electron microscope (TEM). In this test, an atomic force microscopy (AFM) cantilever connected to a Li rod was used to conduct lithiation and subsequently apply tension to the nanowire.[28] While the TEM experiment can provide desirable information such as fracture strength and Young's modulus of nanowires, the electrochemical conditions cannot be controlled, which results in divergent results in literature.[29] Ex-situ nanoindentation and AFM experiments have been employed in the characterization of battery materials, owing to the simplicity of the test, the resolution being suitable to the size of the electrode constituents, and the ability to access a range of material behaviors.[30–33] In-situ AFM is an effective technique to examine the solid electrolyte interface (SEI) layer and the morphological evolution of electrodes during electrochemical cycles.[34] One study tracked the volumetric expansion and the thickness of SEI of Si thin-film electrodes, and explained the capacity hysteresis due to the coupling between the electrochemical potential and mechanical stresses.[35] Another study used in-situ AFM to investigate the distribution of elastic modulus of the SEI across the sample surface; close inspection of the load-displacement curves indicated that the SEI structure is highly heterogeneous, composed of a combination of multiple layers, hard particles, and bubbles.[36] Application of in-situ AFM to study the mechanics of electrode materials is, nonetheless, scarce. One report characterized Si nanopillars in an electrochemical cell in a dry room.[37] Although results provide qualitative information on the influence of lithiation on the mechanical properties, the data exhibited excessive noise which makes the data interpretation elusive.[37] Thus, while AFM is an outstanding tool for probing the morphology of relatively soft materials, nanoindentation is better suited for studying the mechanical response of active materials in batteries, which are in general of high mechanical strength.

Nanoindentation is a well-established technique to measure a variety of mechanical properties of materials at the local positions. The experimental setup requires careful control of the stability of the surrounding environment, sample size and properties, surface condition, and tip size and geometry. Additional challenges are associated with probing materials submerged in a fluid cell environment. When it comes to operando indentation in the course of electrochemical reactions, specific challenges, such as the volumetric change of electrodes during indentation, the substrate effect, structural degradation of the electrodes, and the interference of SEI must be addressed. The goal of this paper is to demonstrate the feasibility of operando indentation to obtain reliable mechanical measurements not

---

[*] Electrochemical Society Member.

[z] E-mail: kjzhao@purdue.edu

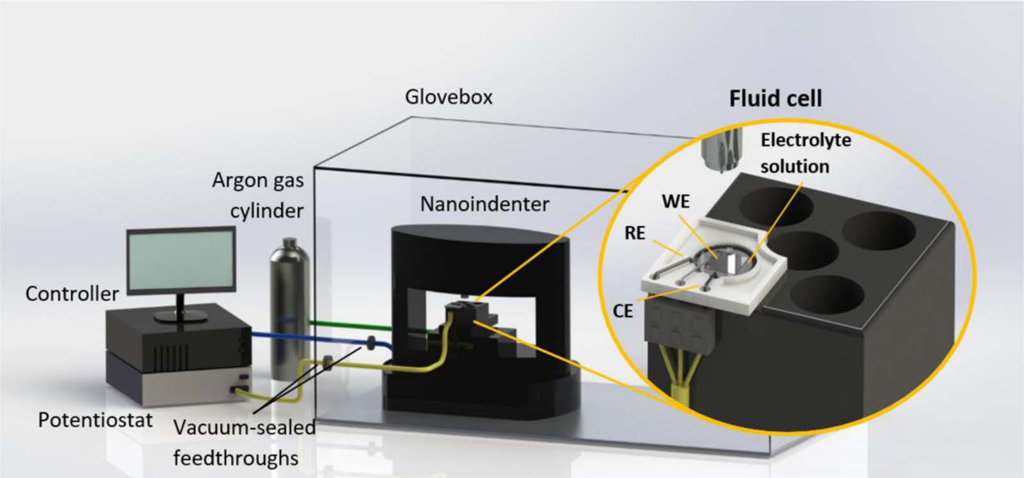

Figure 1. The experimental platform of operando indentation including a nanoindenter residing in an argon-filled glove box, a home-developed liquid cell, and an electrochemical station. The dynamic evolution of the mechanical properties of the working electrode (WE) is probed by nanoindentation during real-time electrochemical reactions.

only in situ, but also during battery operation under various charging rates.

We integrate a nanoindenter, a home-developed fluid cell, and an electrochemical station into an argon-filled glove box. Nanoindentation tests are performed on the electrode submerged in the electrolyte solution as the cell is (dis)charged in an open configuration. We evaluate the influence of the argon environment, electrolyte solution, structural degradation and volumetric change of electrodes upon Li insertion, and the effects of SEI and the substrate. Results inform on the system limitations and capabilities, and provide guidelines on the best experimental practices. Finally, we measure the dynamic evolution of the elastic modulus, hardness, and creep stress exponent of lithiated Si as a continuous function of Li concentration under open circuit as well as various charging rates. The elastic modulus and hardness of lithiated Si steadily decrease as Li reaction proceeds. A power-law relationship between the strain rate and hardness is obtained, with stress exponents of 50 for pristine Si, 22 for lithiated Si of a wide range of Li compositions, and 8 for pure Li. The creep behavior of Si changes dramatically during the first 5% of lithiation and remains mostly invariant in the subsequent lithiation process. The results are in good agreement with prior reports and provide a map of mechanical properties of Si in a complete process of Li insertion.

Experimental Methods

The experimental platform integrates a Keysight G200 nanoindenter equipped with continuous stiffness measurement (CSM), a Princeton VersaSTAT3 electrochemical station, and a home-developed fluid cell into an argon-filled glove box (O_2 and $H_20 < 1$ ppm), Figure 1. The fluid cell is made of Teflon, which is chemically inert to the liquid electrolyte. The height of the fluid cell is carefully designed in order to maintain sufficient liquid electrolyte to fully cover the electrodes, and also to avoid the interference with the motion of the indenter tip, allowing the stage to travel freely from the indenter to the microscope for surface inspection. The sample under investigation is fixed to the center of the fluid cell and serves as the working electrode (WE), while Li metal ribbons are used as the reference (RE) and counter (CE) electrodes fitting inside the slots surrounding the cell. The reference and counter electrodes will not interfere with the indentation of the working electrode. The selected electrolyte, 1M $LiPF_6$ in propylene carbonate (PC) is nonvolatile, enabling a constant fluid level and salt concentration during long tests; preliminary tests using relatively volatile solvent diethyl carbonate (DEC) show more noise and variation in the experimental results.

We first perform control experiments to validate the custom work condition of nanoindentation. Figure 2 shows the comparisons of the elastic modulus of fused silica and amorphous silicon measured in the air versus argon environment, in the standard holder versus the dry fluid cell, and on dry material versus wet sample submerged in the electrolyte-filled fluid cell. The different measurements show close values in the various configurations. The consistent results confirm that the effects of the dielectric constant of Ar on the capacitance gauge of nanoindentation, the non-standard sample holder, and the buoyance and surface tension of the liquid electrolyte are negligible. For the best practice, the enclosure should be solely dedicated to the indentation experiments, since any gas refilling or environmental fluctuation during test may induce excessive noises.

Sample preparation.—Amorphous Si and Li metal are the samples to be characterized. High-purity Li metal ribbons (99.9%, 0.75 mm thick, Sigma-Aldrich) are used, whereas a-Si thin films are prepared using the Leybold E-beam Evaporator. The fabrication starts with the deposition of a 50 nm Ti thin film onto a 1 mm thick silica substrate, followed by the deposition of a 300 nm copper film, both at a rate of 0.5 Å/s. The Cu film serves as the current collector, and the Ti underlayer is used to improve the adhesion between the Cu film and the glass substrate. Finally, a 500 nm Si film is deposited at the same rate of 0.5 Å/s. In addition, a second silicon film, 1.4μm thick, is fabricated for the evaluation of the substrate effect in indentation measurements. The fabrication followed the same procedure, except that the deposition rate of the thick Si film is 1.5 Å/s. The amorphous structure has been

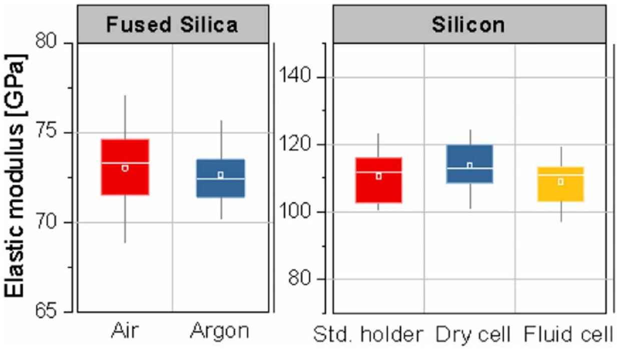

Figure 2. Control experiments performed on fused silica and Si thin film show that indentation tests are not affected by the argon atmosphere, customized holder (dry cell), or the liquid electrolyte environment (fluid cell).

verified in many previous studies for E-beam evaporation of Si films under similar conditions.[38,39]

Concurrent nanoindentation and galvanostatic charge-discharge.—Nanoindentation is performed on a silicon electrode undergoing electrochemical reactions. Tests are conducted uninterruptedly with a grid spacing of 40 μm between indents. Separate, ex-situ measurements (33 indents for one indentation depth) are performed on Li metal ribbons on a standard holder.

The CSM method is used for hardness and modulus measurements (2 nm harmonic displacement, 45 Hz frequency). Tests followed a typical chronology: Indenter approaches material until surface is detected (detection criteria: contact stiffness $S > 200$ N/m), loads at a constant strain rate (0.05 s^{-1}), holds at the maximum load for a dwell time (10 s), partially withdraws and holds the constant load for a second dwell time (60 s) to measure the drift-rate, and finally completely withdraws from the sample. The hardness H and elastic modulus E are given by:

$$H = \frac{P}{A_C}, \qquad [1]$$

and

$$\frac{1}{E_r} = \frac{1-v^2}{E} + \frac{1-v_i^2}{E_i} \qquad [2]$$

where P is the load, v and v_i are the Poisson ratio of the sample and the indenter, respectively, E_i is the elastic modulus of the indenter, and $E_r = 0.5S\sqrt{\pi/A_c}$. The Poisson ratios of 0.22 and 0.3 are specified for Si and Li, respectively.[40] The area of contact A_c is calibrated using the standard fused silica sample. The area function for a Berkovich indenter is $A_c \sim 24.5h_c^2$,[41] where the contact depth h_c is calculated from the absolute tip displacement h, and $h_c = h - 0.75P/S$.[42] In quasi-static indentation tests, the stiffness S is given by the slope of the load-displacement curve during tip removal, while in the continuous stiffness measurement (also known as dynamic instrumented indentation), the stiffness is derived from the in-phase material response to the superimposed oscillating signal.[43]

The constant load and hold method (CLH) is used for creep measurements, for which both the dynamic (CSM) and quasi-static (QS) instrumented nanoindentation are employed.[44] The QS test is preferred over CSM for tests of relatively short hold period to avoid the additional noise from CSM.[40] CSM experiments are conducted for a relatively longer hold period; the results are used to cross-validate the output of the QS measurements. For both tests, the tip is loaded until the maximum indentation depth is reached (100 nm for Si electrode and 3 μm for Li metal), the load is maintained constant for a period of hold time while the tip displacement is measured. Figures S1a and S1b summarize the procedure used for the determination of the creep stress exponent. The tip displacement measured during the peak load is fitted with a Belehradek function[40] (Figure S1a). The data from QS measurements is fitted up to 20 s for Si thin film and 300 s for Li metal, where the creep rate is larger compared to the typical thermal drifts. The time derivative of the fitted curve, $\dot{h}$, divided by the tip displacement h, gives the indentation strain rate $\dot{\varepsilon}_i = \dot{h}/h$.[45] The stress exponent n in the creep power-law is obtained by the slope of the logarithmic plot of hardness, H, versus the indentation strain rate $\dot{\varepsilon}_i$ (Figure S1b):

$$\dot{\varepsilon}_i = C_1 H^n. \qquad [3]$$

This relationship is analogous to the dependence of strain rate $\dot{\varepsilon}$ on the applied stress σ in uniaxial creep tests ($\dot{\varepsilon}_u = C_2\sigma^N$), where C_1 and C_2 are both constants and N is the stress exponent. Despite the large difference in the test methodology, it has been shown that, under steady state conditions (hardness is constant for a constant strain rate), the exponents N and n are close for the same materials.[44–47] Note that Equation 3 requires the hardness to be measured throughout the hold period; this is not practical in QS nanoindentation because the unloading stiffness is undetermined during the hold period. Prior research has shown that the nominal pressure p_{nom}, which is determined directly from the total indentation depth h, $p_{nom} \cong P/24.5h^2$, can be used to accurately estimate the stress exponent.[44,48] Once the elastic transient deformation dissipates, the hardness is a linear function of the nominal pressure, $H = C_3 p_{nom}$, where C_3 is a constant. This relationship yields the strain-rate $\dot{\varepsilon}_i = C_1 C_3^n p_{nom}^n$. Here we have employed the nominal contact pressure in QS tests for the creep characterizations. We use the CSM along with the Maier method[49] in longer hold-period tests to cross-validate the results. The holding times of 300 s and 600 s are set for partially lithiated Si and Li metal, respectively. After long hold times, the creep rate is comparable to the thermal drift. The thermal drift correction cannot effectively rectify the data if the drift rate is not constant throughout the hold period. The CSM method offers the advantage of the continuous measurement of the stiffness, which allows the area of contact during the hold time to be extracted from the Sneddon's equation: $A_c = (S\sqrt{\pi}/2E_r)^2$. Once the contact area is obtained, the hardness is the load divided by the contact area. The tip contact displacement h_c is numerically solved from the area function to determine the strain-rate ($\dot{h}_c/h_c$). We find that the stress exponents obtained using the CSM with long hold periods are close to those of QS measurements with short hold periods (details in Elastic modulus, hardness, and creep stress exponents of Li_xSi and Li metal section).

Galvanostatic lithiation is employed for operando indentation. Continuous measurements of elastic modulus, hardness, and creep stress-exponents are performed during the first galvanostatic discharge (cutoff voltage of 0.01 V vs Li/Li^+) of Si. Elastic modulus and hardness are measured at intermediate lithiation rates (C/10.6 and C/2.9) while creep stress-exponent experiments are conducted at slow discharge rates (C/30 and C/20). Titration experiments in which the galvanostatic discharge and open circuit are alternated are also performed. The test procedure is summarized in Figure S2, showing a complete set of electrochemical (voltage and current profiles) and indentation data (drift-rate, elastic modulus, and hardness) as a function of the discharge time. In addition, electrochemical cycling is employed to evaluate the relation between the drift-rate and the applied current at high C-rates (C/1.5 and C/3.3).

Li concentration is calculated from the state of charge of lithiated Si (assuming a lithiation capacity of 3579 mAh/g for Si). This estimation assumes a homogeneous distribution of Li throughout the sample. Note that the local Li concentration near the indenter tip may deviate from the nominal concentration as the stress field may alter the chemical potential of Li. The inhomogeneity of Li distribution near the tip depends on the Li diffusion rate, the indentation time, and creep properties of lithiated silicon.

Challenges of operando Measurements

Structural degradation of electrodes.—In instrumented nanoindentation, the area of contact is derived from the displacement of the tip into the surface as opposed to directly imaging the residual impression. The accuracy of the result depends on the sample surface being approximately flat and continuous. For instance, indenting on top of a discontinuity such as a crack would lead to uninterpretable results. Since Si is known to undergo significant volumetric expansion and structural degradation during lithiation reactions, we monitor the integrity of the surface via optical microscope before and after tests. Figure 3 shows the representative optical images of the surface of the Si film during the first electrochemical cycle (video in the supplementary information). During Li insertion, the in-plane expansion of Si thin film is constrained by the substrate, leading to high compressive stresses which suppress crack nucleation and growth, Figures 3a, 3b, and 3c. Pre-existing local imperfections are amplified during lithiation. However, most of the regimes are maintained in good conditions, allowing grid indentation to be performed over a large area. A small percentage of compromised tests (< 4% of all tests) falling nearby the local imperfections are easily identifiable and are removed from the results. Delithiation starts once the voltage cutoff for lithiation is reached. During Li extraction, Si shrinks and the stresses switch the sign from compressive to tensile which drive cracks formation and propagation, Figure 3d. We observe that the first set of cracks

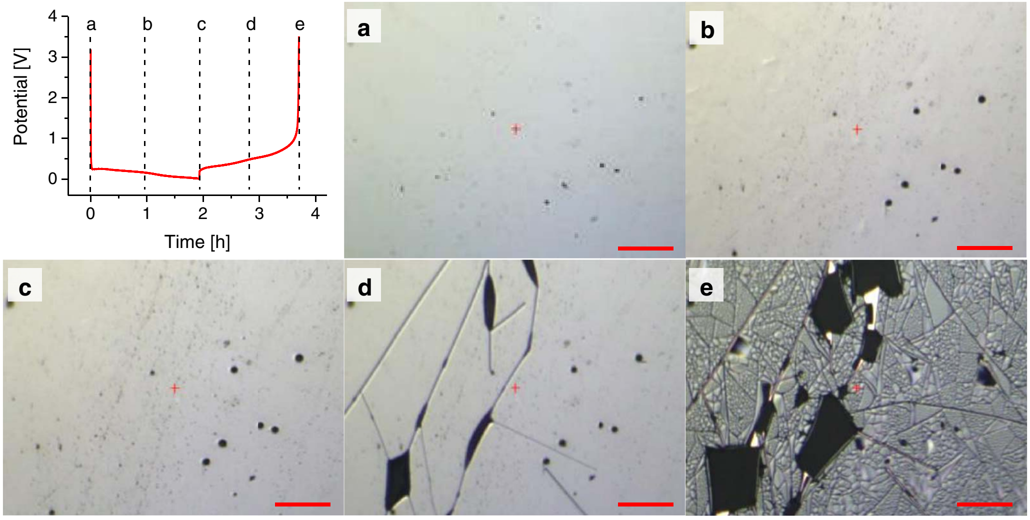

Figure 3. Optical images of the surface condition of a silicon thin film electrode during the first cycle at the charging rate C/2 (scale bars correspond to 100 μm). During lithiation (a, b, c), there is no evidence of mechanical failure and the surface is adequate for indentation tests. During delithiation (d, e), the thin film is cracked and delaminated.

generally develop between 25–65% of delithiation and grow and widen as delithiation proceeds, Figure 3e. Most damages occur at the final 15% of delithiation, resulting in massive delamination of the thin film from the substrate (appears as dark regions in optical images due to light deflection) and/or extensive formation of micron-sized islands. In this work, we limit the mechanical measurements to the first lithiation to avoid excessive cracking and SEI growth. For the interest of investigating mechanical behaviors of Si in the course of charge and discharge cycles, the structural integrity of the sample could be preserved by providing relatively narrow electrochemical windows.

Volume expansion of electrodes during indentation.**—**Si expands during operando indentation while Li inserts. The indenter displacement into the surface of the sample is determined by subtracting the tip displacement before contact from its entire moving distance. If the sample changes in size when the tip is reaching the specified maximum load or displacement, the estimated contact depth, and consequently the area of contact, is inaccurate. Here we evaluate (1) the drift caused by the volumetric change of electrodes during Li reactions, so-called electrochemical drift as an analogy to the thermal drift, and (2) the effectiveness of the conventional thermal drift correction to treat the electrochemical drift.

We first evaluate the electrochemical drift at different charging rates. For the sake of estimation, let's assume $h_c \cong h$ and $A_c \cong 24.5\,h^2$, therefore,

$$H^{Error} = \frac{H_M - H_T}{H_T} = \frac{\left(\frac{P}{A_M} - \frac{P}{A_T}\right)}{\frac{P}{A_T}} = \frac{\left(\frac{1}{h_M^2} - \frac{1}{h_T^2}\right)}{\frac{1}{h_T^2}}. \qquad [4]$$

The subscripts "M" and "T" stand for the measured and true values, respectively. The relationship between the measured and the true indentation depth (inset schematic in Figure 4a) is $h_T = h_M + \dot{d}\Delta t$, where h is the indentation depth, $\dot{d}$ is the rate of change of the sample thickness, and Δt is the elapsed time from the tip in contact with the sample surface. Simplifying Equation 4 and putting it in terms of measured tip displacement h_M, the error in the hardness H due to the volume expansion of Si is:

$$H^{Error} = \left(\frac{h_M + \dot{d}\Delta t}{h_M}\right)^2 - 1. \qquad [5]$$

Similarly, the error in the elastic modulus E can also be estimated:

$$E^{Error} = \left(\frac{h_M + \dot{d}\Delta t}{h_M}\right) - 1. \qquad [6]$$

The relationship between the volume expansion of Si and the degree of lithiation is approximately linear.[35] Assuming the film only expands out-of-plane, the present thickness d is given by $d = d_o(1 + \beta z)$, where d_o is the initial thickness and z defines the state of charge with 0 representing the pristine Si and 1 being the fully lithiated state. Yoon et al. measured this relationship for a-Si film in the $LiPF_6$-PC electrolyte and found the expansion coefficient of $\beta = 2.81$.[35] For galvanostatic charging, the state of charge is given by $z = \frac{i}{Q}t$, where i is current, Q is the charge capacity of the Si electrode, and t is the charging time. Taking the time derivative of the film thickness d, it gives the rate-of-change in film thickness with respect to the charging rate:

$$\dot{d} = \beta d_0 \frac{i}{Q}. \qquad [7]$$

As i/Q dictates the charging rate C_{rate}, the combination of Equations 5, 6 and 7 offers an estimate of the error in indentation introduced by sample expansion/shrinkage as a function of the charging rate. Figure 4a shows the estimated error in hardness and elastic modulus for $d_0 = 500\ nm$, $\Delta t = 70$ s, and $h_M = 100\ nm$, which are typical values in the nanoindentation experiments. The results show that the error, if the electrochemical drift is not corrected, can be significant (more than 10%), especially for the measurements of the charging rate over C/4. For the intercalation-type electrodes, the volumetric expansion is small and has negligible effects on hardness and modulus measurements. However, for the insertion- and conversion-type high capacity electrodes such as Si,[50] the electrochemical drift, in particular during fast charging, is significant. We need to establish a procedure to account for the electrochemical drift in order to investigate the mechanical behaviors of materials at non-equilibrium chemical states.

Thermal drift correction is a conventional method to analyze the tip displacement when the sample is undergoing volume changes during indentation.[41] For example, in high-temperature measurements, the temperature difference between the tip and the sample may lead the material around the tip to expand or shrink.[51] The schematic in Figure 4b illustrates the correction procedure (the drift-rate is exaggerated in the illustration). During the thermal drift period, step 4 in a typical test chronology, the load (red line) is maintained constant while the tip displacement (continuous blue line) is measured. The rate of change in tip displacement with time gives the thermal drift-rate, $\dot{h}_d$. This value, multiplied by the elapsed time, is subtracted from the indentation depth h_M which gives the corrected tip displacement $h_{corrected}$ (dotted blue line). Notice that the correction is only effective

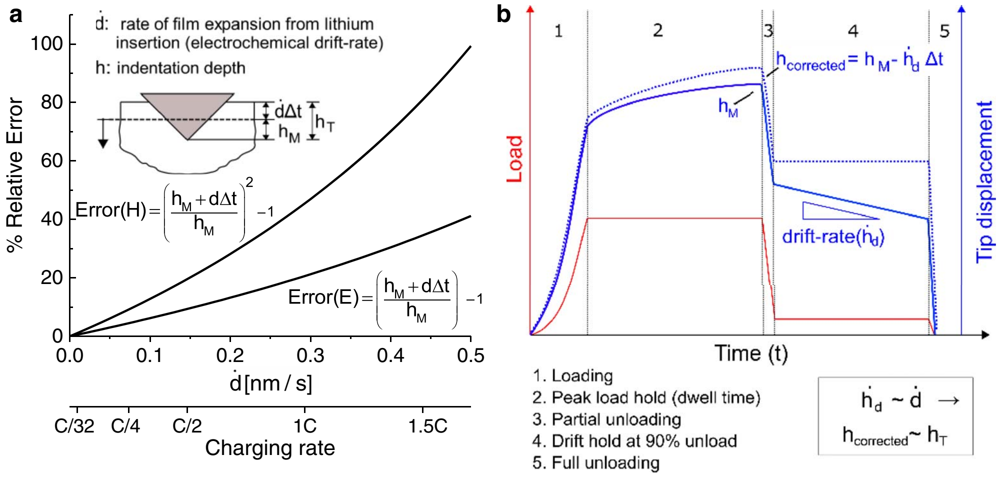

Figure 4. (a) The relative errors in the elastic modulus and hardness induced by the volumetric change of Si during operando indentation. (b) The correction of the electrochemical drift in analogy to the thermal drift. Control experiments are performed to minimize the effects of the environment such as vibration and temperature fluctuation. Sufficient dwell time is allowed for the material to creep to a negligible rate before unloading. The measured drift is attributed to the volumetric change of the thin film electrode during electrochemical reactions.

if the drift is approximately linear during the entire time of the test. A negative drift in the tip displacement (negative slope in step 4) means that the tip is withdrawing from the sample, that is, the sample is expanding toward the tip making the tip retreat in order to maintain the contact area constant and thus the constant load. Likewise, a positive drift (positive slope in the tip displacement) indicates that the sample is shrinking. The drift can be attributed to the electrochemical expansion upon Li insertion or extraction if the residual creep, thermal fluctuations, and the change of mechanical properties of the sample during the indentation test are negligible. Here we investigate the electrochemical drift by designing the experiments of minimized environmental fluctuations (long stabilization time, no air flow, vibration isolation, and temperature controlled environment) and sufficient dwell time. In this case, the measured drift-rate $\dot{h}_d$ is mostly attributed to the electrochemical drift-rate $\dot{d}$ by Li insertion (Figure 4).

Figures 5a and 5b show the drift rates of Si (red dotted lines) during the titration experiments (blue solid lines) under a relatively slow cycle (C/3.3) and a relatively fast charging case (C/1.5), respectively. Results clearly show that the drift-rate (volume change) is practically zero under the open circuit condition when zero current is provided, negative for a negative current (lithiation), and positive for a positive current (delithiation). It is also noteworthy that at the moment immediately after that the current is applied, an electrochemical shock of excessive tip motion is persistent. The electrochemical drifts gradually reach steady values following the initial "shock". The effect is not well understood at this writing, possibly due to the drastic

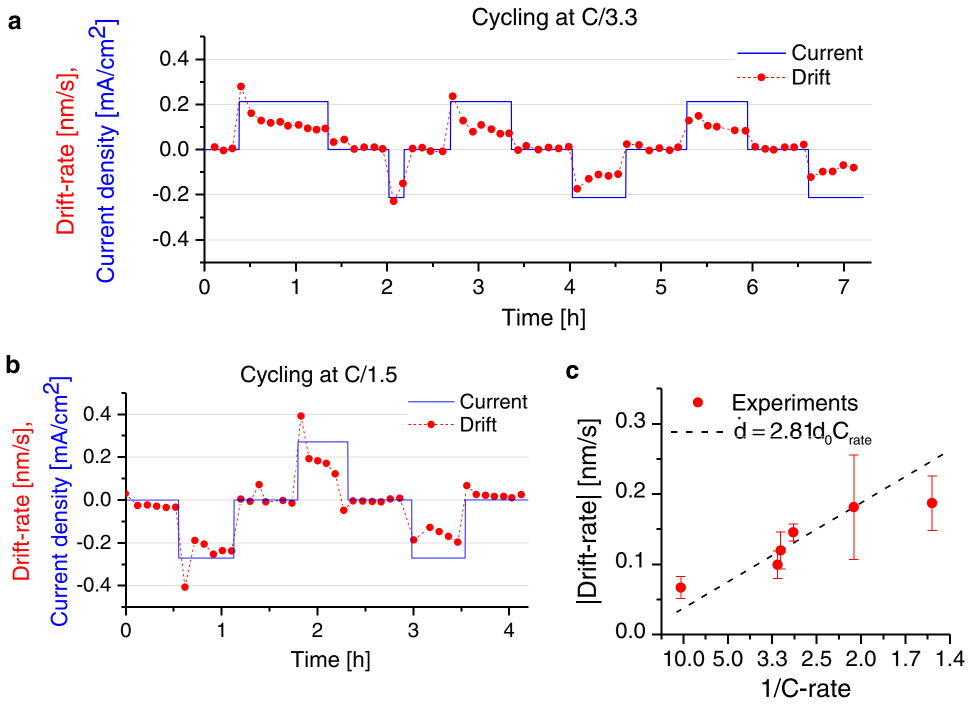

Figure 5. Electrochemical drift (red dots) measured during titration galvanostatic (de)lithiation (blue lines). (a) Cyclic test at C/3.3 charging rate, (b) cyclic test at C/1.5, and (c) the comparison of the drift rates with the theoretical prediction.

structural rearrangements of the host material upon the application of the current or the large compressive stress that may facilitate material pile up around the indenter. Figure 5c depicts the average electrochemical drift rate $\dot{h}_d$ (red dots) (excluding the peaks resulted from the electrochemical shocks) as a function of the C-rate. The experimental output is in good agreement with the theoretical prediction of $\dot{d}$ in Equation 6. The electrochemical drift rate is on the same magnitude of the typical thermal drift in high-temperature tests (~0.2 nm/s)[51] that the thermal drift correction can be an effective way to account for the volumetric change of electrodes during electrochemical reactions. Although the electrochemical drift and the thermal drift can be separately measured as shown in Figures 5a and 5b, it is not necessary to separate these two origins of drift and the standard correction procedure outlined in Figure 4 is sufficient to account for both effects.

Interference of surface layer and substrate effect.—A challenge of the operando measurement is the presence of the SEI layer on top of the Si sample. We will evaluate the potential interference of the surface layer in nanoindentation. The substrate effect is not a particular problem of operando indentation, nevertheless, it is a common issue in the characterization of thin films and its assessment is important in the data interpretation. The continuous stiffness measurements are helpful in assessing the SEI and the substrate effects in which the elastic modulus and hardness are measured continuously as a function of the indentation depth.

The thickness of the SEI of Si, ranging from a few to several tens of nanometers, largely depends on the choice of the liquid electrolyte. Yoon et al. determined the SEI thickness of Si in the half-cell composed of amorphous Si/LiPF$_6$-PC electrolyte/Li metal using in-situ AFM measurements. They found that the SEI thickness by the end of the first lithiation is less than 5 nm and is ~10 nm after the first cycle.[35] Another report by Zheng et al. found that the SEI structure formed on Si is significantly inhomogeneous across the electrode surface. The elastic moduli of the constituents of SEI are typically below 1 GPa with peak values around 4 GPa.[36] The SEI is considerably more compliant than lithiated Si. We assess if the presence of SEI would lead to the overestimation of the contact area between the tip and the Si film. Equation 2 provides the contact stiffness as a function of indentation depth in a material of a given elastic modulus. For the SEI layer of thickness 10 nm and typical modulus 1 GPa, the contact stiffness of approximately 60 N/m is obtained which is considerably lower than the surface detection criteria $S > 200$ N/m. Thus, the measured indenter displacement should be insensitive to the compliant SEI layer and the influence of SEI in our experiments can be neglected. It is worth reiterating that SEI is a complex issue and its thickness can be substantially different under different cyclic conditions. One study reported that the SEI thickness is ranging from 7 to 20 nm depending on the electrochemical window, temperature, and electrolyte additives.[36] In operando indentation, a few approaches can be used to mitigate the effect of SEI such as increasing the indentation depth, using larger contact stiffness for surface detection, and narrowing the electrochemical window. The capability of CSM measurements to acquire mechanical properties as a function of the indentation depth is useful in detecting the SEI effect. A plot of the elastic modulus and hardness versus indentation depth would display a large change in slope as the indenter crosses a softer SEI layer into a much stiffer electrode.

The substrate effect mainly depends on the ratios between (1) the indentation depth and the film thickness, and (2) the mechanical properties of the film and the substrate. A general rule is that the indentation depth of less than 10% of the film thickness can minimize the substrate effect.[52,53] In our experiments, 80 nm is about the shallowest indentation depth below which excessive noise would compromise the precision of the tests. Figure 6 compares the modulus and hardness of a thin Si film (initial thickness of 0.5 μm and ~1.6 μm after full lithiation) and a thicker film of 1.4 μm thickness. The thick film was not suitable for operando tests as it experiences enormous structural degradation upon lithiation and is only used to evaluate the substrate effect. Figure 6 shows the modulus and hardness measured at different indentation depths by CSM for the two Si samples. The thin film is apparently much more sensitive to the substrate. When the thin film is lithiated and expands in its thickness, the substrate effect is mitigated. The slope of elastic modulus with respect to the indentation depth changes its sign from negative to positive when Si is fully lithiated, which is a result of the film being initially stiffer than the silica substrate, but more compliant by the end of the lithiation (elastic moduli for pure Si, fully lithiated Si, and silica substrate are about 110 GPa, 50 GPa, and 70 GPa, respectively). At the indentation depth of 80 nm, the hardness of the thick and thin samples is about to converge while the elastic modulus differs by around 10%. The comparison suggests that the deviation of the elastic modulus measurements for the thin Si film upon lithiation is bounded at approximately 10%, which agrees with the models of substrate correction.[54–56] The application of substrate correction using the established models would require simplifying the underneath Cu, Ti, and silica multilayers to a single layer. In this work, we opt for presenting raw measurements while acknowledging the bounded uncertainty resulted from the substrate effect.

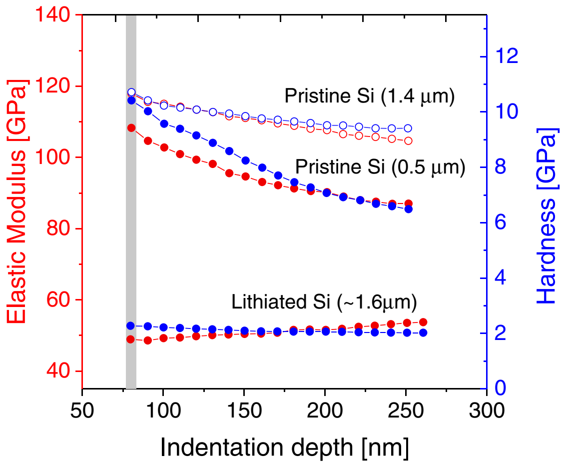

Figure 6. Elastic modulus and hardness as a function of the indentation depth for the Si films of 0.5 μ*m* (~1.6 μ*m* after lithiation) and 1.4 μ*m* thickness. The slopes indicate the dependence of the measurements on the film thickness and properties of the substrate. The indentation depth 80 *nm* (gray line) is selected as a balance between the experimental accuracy and minimization of the substrate effect.

Elastic Modulus, Hardness, and Creep Stress Exponents of Li$_x$Si and Li Metal

We measure the continuous evolution of the mechanical properties of Si in the course of Li reactions using operando indentation. We focus on the effects of (1) the Li composition, and (2) the charging rate on the mechanical behaviors of lithiated Si. Li metal ribbons are tested separately in a standard holder. The supplementary information Figures S4 shows the load-displacement curves of lithiated Si of different Li compositions. The elastic modulus, hardness, and creep stress exponent as a function of Li concentration are shown in Figures 7a, 7b, and 7c, and the comparisons with literature data are shown in Figures 7d, 7e, and 7f, respectively. Tests performed under the open circuit (O.C.) condition are presented with averages and standard deviations, while the single data points for different charging rates during cell operation represent individual indentations.

The elastic modulus and hardness are measured using CSM. The modulus and hardness of pure Li (green star in Figures 7a and 7b) are 8.53 GPa and 28 MPa, respectively. The elastic modulus is close to the uniaxial tensile test result which is 7.8 GPa.[57] The supplementary information Figure S3a shows the load-displacement curves for indention of Li metal at different indentation depths, and Figure S3b shows the elastic modulus and hardness of Li metal as a function of the indentation depth. The large standard deviation is possibly caused

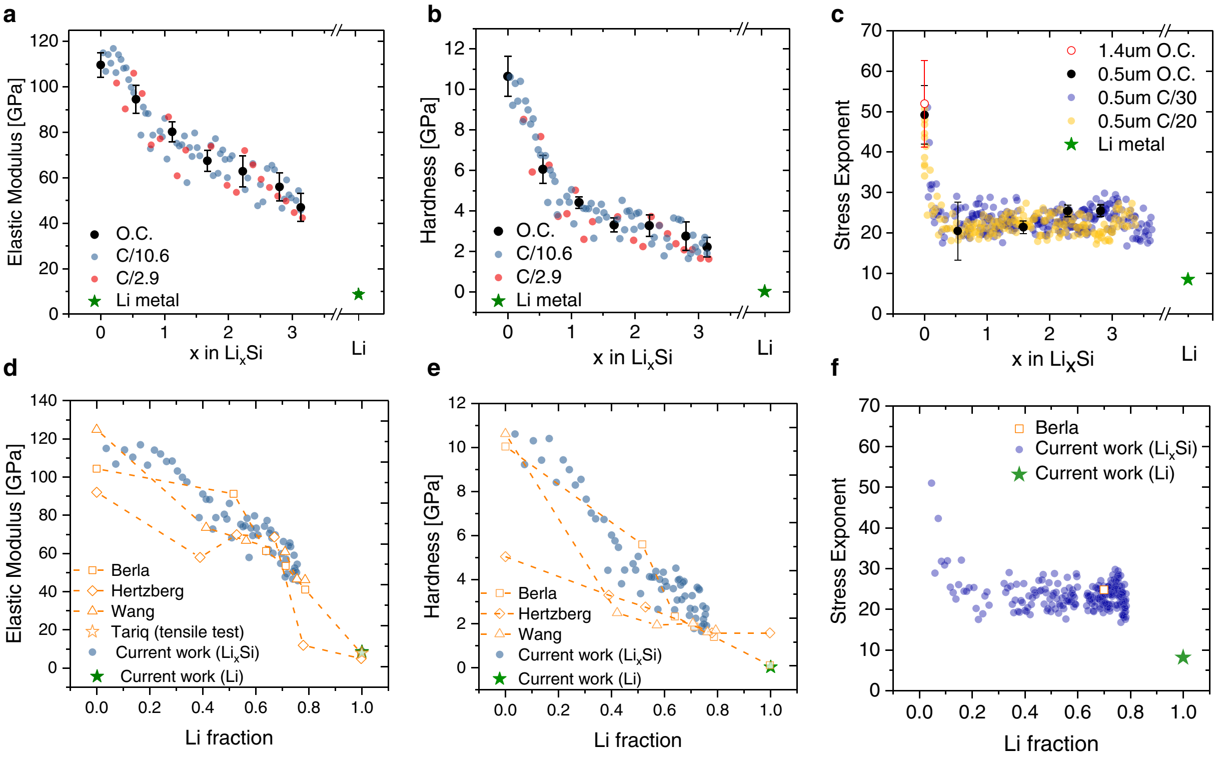

Figure 7. Elastic modulus, hardness, and stress exponent of Si (solid dots) measured as a function of Li concentration in open circuit (O.C.) and under various charging rates (a, b, c). The comparison of current work with the literature results by Wang et al.,[58] Hertzberg et al.,[30] Berla et al.,[40] and Tariq et al.[57] (d, e, f). Separate measurements performed on pure Li metal are included (green star).

by the surface roughness of the Li sample, Li creep, and material pile-up near the indentation tip. For lithiated Si, the elastic modulus and hardness steadily decrease with Li concentration. The elastic modulus drops from approximately 110 GPa for pristine Si to 47 GPa for $Li_{3.2}Si$ (52% reduction), while the hardness decreases from 10.6 GPa to 2.2 GPa (78% reduction). The results are well within the range reported by ex-situ measurements,[30,40,58] confirming that the SEI layer has a negligible effect on the operando measurements and that the surface quality is sufficient for indentation tests. The comparisons with literature also clearly show the advantage of the uninterrupted tests. In ex-situ experiments, multiple samples are charged up to a specific state-of-charge, removed from the cell, and tested using different means to suppress oxidation such as covering the sample with inert oil and providing a continuous flow of inert gas. It appears that the variation of the experimental procedures may introduce some unnatural transitions in the mechanical properties during lithiation which makes data interpretation difficult. Our operando indentation results show the continuous and smooth decrease of the modulus and hardness of lithiated Si, and the rule of mixture provides a reasonable approximation to capture the dynamic evolution of the mechanical properties.

Figures 7c and 7f depict the stress exponent of lithiated Si as a function of the Li composition under different charging rates. The results are obtained from the constant-load hold quasi-static measurements (load-displacement curves at various Li concentrations are shown in Figure S4). The stress exponent for pure Si is approximately 50, or equivalently, the strain rate sensitivity is 0.02, with 0 meaning that the stress response is insensitive to the strain rate, and 1 representing Newtonian viscous flow. The comparison between the 0.5 μm (solid black circle) and the 1.4 μm (open red circle) thick pristine films indicates that the stress exponent is not significantly influenced by the substrate. The creep of lithiated Si behaves like a step function – the stress exponent dramatically decreases upon the start of lithiation and drops to 22 for $Li_{0.5}Si$. Afterwards, the stress exponent remains nearly constant for the Li composition over $Li_{0.5}Si$. A prior first-principles modeling demonstrated that the brittle-to-ductile transition occurred in $Li_{0.25}Si$ where a small fraction of Li mediated the flow of lithiated Si.[59] This transition is corroborated by our measurements of the stress exponents. The constant strain-sensitivity of lithiated Si over a wide range of compositions is intriguing and its mechanistic understanding remains to be explored in a future study. The stress exponent of approximately 22 for lithiated Si is in close agreement with ex-situ nanoindentation measurements reported by Berla et al.[40] Other studies[57,60,61] on the viscoplastic properties of Li metal and lithiated Si adopted power-law type constitutive equations ($\dot{\varepsilon} = A(\sigma - \sigma_o)^{\delta}$) using the overstress instead of the absolute stress ($\dot{\varepsilon} = B(\sigma)^n$), where A and B are constants, σ is the flow stress, σ_o is a reference stress, δ is the overstress exponent, and n is the conventional stress exponent. We want to point out this detail because the stress exponent and the overstress exponent are not equivalent. Normalizing the stress and strain rate, nevertheless, does not change the value of the exponent. The reported values of δ for Li metal from uniaxial tensile experiments at various strain rates[57] and indentation tests at constant loading rate[60] are 1.75 and 1.85, corresponding to the stress exponents n of 11.9 and 9.0, respectively. These values are consistent with the result obtained in this work which is about 8.1. We compare the QS creep results with the CSM output using the Maier method.[49] The stress exponent of partially lithiated Si is 20.4 for the holding time of 300 s, while the stress exponent of Li metal obtained from the 600 s holding is 8.77.

We observe that the elastic modulus and hardness of lithiated Si for a given composition measured at different charging rates and under open circuit condition are nearly identical, Figures 7a and 7b. A few earlier studies proposed the dependence of the mechanical properties of electrodes on the charging rate. Brassart and Suo[22] postulated that under the non-equilibrium chemical state, the chemical driving force for reactions in a solid perturbs the valence states of the reactants and enables a material to flow under a lower level of stress than that at the chemical equilibrium state. Zhao et al.[62] found that the wafer curvature measurement of the biaxial stress in Si thin films cycled at 1C was lower than the yield strength obtained from first-principles modeling, and attributed such difference to this coupling between reaction and plastic flow (reactive flow). The coupling of chemical reactions and plasticity has also been studied by recent theories of anisotropic compositional expansion and glassy relaxation.[63,64] The coupling between the mechanical properties and the chemical reaction rate is not apparent in the operando indentation tests. For instance, the hardness, which is typically in a linear relationship with the flow stress, is about the same for the measurements at galvanostatic charging rates of C/2.9 and C/10.6 as well as at open circuit condition. This finding, however, does not exclude the possible coupling between the mechanical behaviors and the reaction rate in electrodes. With the relative slow charging rates, the coupling effects may be convoluted with the variation of the experimental output, or the timescales for the chemical reaction and plastic flow of lithiated Si may be vastly different which makes it difficult to capture by nanoindentation. Further investigation considering a wider span of charging rates and different materials is necessary to make more conclusive assessments of reactive flow and will be a topic for another study. It is also worth noting that wafer curvature experiments on Si found that the flow stress increased by 0.1 GPa when the charging rate increased from C/128 to C/2.[65] Pharr et al. attributed this effect to the strain-rate sensitivity. In wafer curvature experiments, the substrate bends proportionally to the stress developed in the film electrode, which depends on the rate of Li insertion as well as the viscoplastic properties of the electrodes. In nanoindentation, however, the strain rate and the electrochemical charging rate are separate – the strain rate $\dot{\varepsilon} = \dot{h}/h$ is provided by the load cell while the charging rate is controlled by the electrochemical station. Thus, operando indentations allow the measurement of modulus and hardness of electrodes independently from their viscous behaviors.

Conclusions

In this work, we set forth an operando indentation platform that integrates a nanoindenter, a custom fluid cell, and an electrochemical station in an inert environment. The experiment enables the measurement of the dynamic chemomechanical response of electrodes in an open configuration during real-time electrochemical reactions. We address the technical challenges associated with the custom working environment, the structural degradation and volumetric expansion of the electrodes, and the interference of the surface layer and the substrate effect. We determine the continuous evolution of the elastic modulus, hardness, and creep stress exponent of lithiated Si as a function of Li concentration. The comparisons with the prior reports are discussed and the advantages of the operando indentation are highlighted. operando indentation provides a perfect platform to characterize the chemomechanical behaviors of materials during the dynamic process of electrochemical reactions. In the future, it will help to unravel a variety of phenomena in energy materials involving the intimate interactions between mechanics and electrochemistry, such as stress-regulated ion diffusion and electron transfer,[66] concurrent processes of plasticity and reaction,[62,22] corrosive fracture,[67] and mechanical stability of electrodes in the long-term performance of batteries.[68]

Acknowledgments

This work is supported by the National Science Foundation through the grant CMMI-1726392.

References

1. M. Ebner, F. Marone, M. Stampanoni, and V. Wood, *Science*, **342**, 716 (2013).
2. R. Xu and K. Zhao, *J. Electrochem. Energy Convers. Storage*, **13**, 030803 (2016).
3. S. B. Adler, *J. Am. Ceram. Soc.*, **84**, 2117 (2001).
4. N. Swaminathan, J. Qu, and Y. Sun, *Philos. Mag.*, **87**, 1705 (2007).
5. N. Rolston, B. L. Watson, C. D. Bailie, M. D. McGehee, J. P. Bastos, R. Gehlhaar, J. -E. Kim, D. Vak, A. T. Mallajosyula, G. Gupta, A. D. Mohite, and R. H. Dauskardt, *Extreme Mech. Lett.*, **9**, 353 (2016).
6. M. Stengel and N. A. Spaldin, *Nature*, **443**, 679 (2006).
7. R. D. Mindlin, *Int. J. Solids Struct.*, **5**, 1197 (1969).
8. M. Louthan, G. Caskey, J. Donovan, and D. Rawl, *Mater. Sci. and Eng.*, **10**, 357 (1972).
9. K. Zhao and Y. Cui, *Extreme Mech. Lett.*, **9**, 347 (2016).
10. M. R. Palacin and A. de Guibert, *Science*, **351**, 1253292 (2016).
11. N. Nitta, F. Wu, J. T. Lee, and G. Yushin, *Mater. Today*, **18**, 252 (2015).
12. N. Rolston, B. L. Watson, C. D. Bailie, M. D. McGehee, J. P. Bastos, R. Gehlhaar, J. -E. Kim, D. Vak, A. T. Mallajosyula, G. Gupta, A. D. Mohite, and R. H. Dauskardt, *Extreme Mech. Lett.*, **9**, 353 (2016).
13. A. Mukhopadhyay and B. W. Sheldon, *Prog. Mater. Sci*, **63**, 58 (2014).
14. S. Zhang, K. Zhao, T. Zhu, and J. Li, *Prog. Mater. Sci.*, **89**, 479 (2017).
15. Y. T. Cheng and M. W. Verbrugge, *J. Electrochem. Soc.*, **157**, A508 (2010).
16. K. J. Zhao, M. Pharr, J. J. Vlassak, and Z. G. Suo, *J. Appl. Phys.*, **108**, 073517 (2010).
17. Y. Gao and M. Zhou, *J. Appl. Phys.*, **109**, 014310 (2011).
18. Y. H. An and H. Q. Jiang, *Modell. Simul. Mater. Sci. Eng.*, **21**, 074007 (2013).
19. H. Yang, F. Fan, W. Liang, X. Guo, T. Zhu, and S. Zhang, *J. Mech. Phys. Solids*, **70**, 349 (2014).
20. C. V. Di Leo, E. Rejovitzky, and L. Anand, *Int. J. Solids Struct.*, **67**, 283 (2015).
21. S. M. Khosrownejad and W. A. Curtin, *J. Mech. Phys. Solids*, **94**, 167 (2016).
22. L. Brassart and Z. Suo, *J. Mech. Phys. Solids*, **61**, 61 (2013).
23. S. P. V. Nadimpalli, R. Tripuraneni, and V. A. Sethuraman, *J. Electrochem. Soc.*, **162**, A2840 (2015).
24. M. Pharr, Z. Suo, and J. J. Vlassak, *Nano Lett.*, **13**, 5570 (2013).
25. Y. H. Kim, S. I. Pyun, and J. Y. Go, *Electrochim. Acta*, **51**, 441 (2005).
26. S. I. Pyun, J. Y. Go, and T. S. Jang, *Electrochim. Acta*, **49**, 4477 (2004).
27. D. Li, Y. Wang, J. Hu, B. Lu, Y. -T. Cheng, and J. Zhang, *J. Power Sources*, **366**, 80 (2017).
28. A. Kushima, J. Y. Huang, and J. Li, *ACS Nano*, **6**, 9425 (2012).
29. S. T. Boles, C. V. Thompson, O. Kraft, and R. Mönig, *Appl. Phys. Lett.*, 103 (2012).
30. B. Hertzberg, J. Benson, and G. Yushin, *Electrochem. Commun.*, **13**, 818 (2011).
31. L. S. Vasconcelos, R. Xu, J. Li, and K. Zhao, *Extreme Mech. Lett.*, **9**, 495 (2016).
32. M. Qu, W. H. Woodford, J. M. Maloney, W. C. Carter, Y. -M. Chiang, and K. J. Van Vliet, *Adv. Energy Mater.*, **2**, 940 (2012).
33. K. Zeng and J. Zhu, *Mech. Mater.*, **91**, 323 (2015).
34. A. v Cresce, S. M. Russell, D. R. Baker, K. J. Gaskell, and K. Xu, *Nano Lett*, **14**, 1405 (2014).
35. I. Yoon, D. P. Abraham, B. L. Lucht, A. F. Bower, and P. R. Guduru, *Adv. Energy Mater.*, 6 (2016).
36. J. Zheng, H. Zheng, R. Wang, L. Ben, W. Lu, L. Chen, L. Chen, and H. Li, *Phys. Chem. Chem. Phys.*, **16**, 13229 (2014).
37. Q. P. McAllister, K. E. Strawhecker, C. R. Becker, and C. A. Lundgren, *J. Power Sources*, **257**, 380 (2014).
38. A. Michael, C. Y. Kwok, P. Wang, O. Kazuo, and S. Varlamov, *J. Microelectromech. Syst.*, **24**, 1951 (2015).
39. S. Kugler, G. Molnár, G. Petö, E. Zsoldos, L. Rosta, A. Menelle, and R. Bellissent, *Phys. Rev. B*, **40**, 8030 (1989).
40. L. A. Berla, S. W. Lee, Y. Cui, and W. D. Nix, *J. Power Sources*, **273**, 41 (2015).
41. J. Hay, *Experimental Techniques*, **33**, 66 (2009).
42. W. C. Oliver and G. M. Pharr, *J. Mater. Res.*, **19**, 3 (2011).
43. X. Li and B. Bhushan, *Mater. Charact.*, **48**, 11 (2002).
44. C. Su, E. G. Herbert, S. Sohn, J. A. LaManna, W. C. Oliver, and G. M. Pharr, *J. Mech. Phys. Solids*, **61**, 517 (2013).
45. B. N. Lucas and W. C. Oliver, *Metall. Mater. Trans. A*, **30**, 601 (1999).
46. H. Takagi, M. Dao, and M. Fujiwara, *Mater. Trans.*, **55**, 275 (2014).
47. R. Mahmudi, R. Roumina, and B. Raeisinia, *Mater. Sci. Eng.: A*, **382**, 15 (2004).
48. A. F. Bower, N. A. Fleck, A. Needleman, and N. Ogbonna, *Proc. R. Soc. London Ser. A-Math. Phys. Eng. Sci.*, **441**, 97, (1993).
49. V. Maier, B. Merle, M. Göken, and K. Durst, *J. Mater. Res.*, **28**, 1177 (2013).
50. R. Xu, L. S. Vasconcelos, and K. Zhao, *J. Mater. Res.*, **31**, 2715 (2016).
51. J. M. Wheeler, D. E. J. Armstrong, W. Heinz, and R. Schwaiger, *Curr. Opin. Solid State Mater. Sci.*, **19**, 354 (2015).
52. J. L. He and S. Veprek, *Surf. Coat. Technol.*, **163**, 374 (2003).
53. Y. Sun, T. Bell, and S. Zheng, *Thin Solid Films*, **258**, 198 (1995).
54. J. Hay and B. Crawford, *J. Mater. Res.*, **26**, 727 (2011).
55. H. Gao, C. Chiu, and J. Lee, *Int. J. Solids Struct.*, **29**, 2471 (1992).
56. K. Durst, M. Göken, and H. Vehoff, *J. Mater. Res.*, **19**, 85 (2011).
57. S. Tariq, K. Ammigan, P. Hurh, R. Schultz, P. Liu, and J. ShangMay, In *Particle Accelerator Conference*, **3**, p. 1452, IEEE (2003).
58. X. Wang, S. S. Singh, T. Ma, C. Lv, N. Chawla, and H. Jiang, *Chem. of Mater.*, **29**, 5831 (2017).
59. K. Zhao, W. L. Wang, J. Gregoire, M. Pharr, Z. Suo, J. J. Vlassak, and E. Kaxiras, *Nano Lett.*, **11**, 2962 (2011).
60. Y. Wang and Y. -T. Cheng, *Scr. Mater.*, **130**, 191 (2017).
61. G. Bucci, S. P. V. Nadimpalli, V. A. Sethuraman, A. F. Bower, and P. R. Guduru, *J. Mech. Phys. Solids*, **62**, 276 (2014).
62. K. Zhao, G. A. Tritsaris, M. Pharr, W. L. Wang, O. Okeke, Z. Suo, J. J. Vlassak, and E. Kaxiras, *Nano Lett*, **12**, 4397 (2012).
63. V. I. Levitas and H. Attariani, *Sci. Rep.*, **3**, 1615 (2013).
64. S. M. Khosrownejad and W. A. Curtin, *J. Mech. Phys. Solids*, **94**, 167 (2016).
65. M. Pharr, Z. Suo, and J. J. Vlassak, *J. Power Sources*, **270**, 569 (2014).
66. S. Kim, S. J. Choi, K. Zhao, H. Yang, G. Gobbi, S. Zhang, and J. Li, *Nat. Commun.*, **7**, 10146 (2016).
67. X. Huang, H. Yang, W. Liang, M. Raju, M. Terrones, V. H. Crespi, A. C. T. van Duin, and S. Zhang, *Appl. Phys. Lett.*, 103 (2013).
68. R. Xu, H. Sun, L. S. Vasconcelos, and K. Zhao, *J. Electrochem. Soc.*, **164**, A3333 (2017).